REVIEW

Check for updates

Seaweed residue as a low-cost source for producing cellulose nanofibrils with ultraviolet shielding properties

Shan Jiang,†[a] Xincheng Peng,†[ab] Zixin Wu,[a] Hemin Cui,[c] Ligang Wei,[a] Guolin Shao, [iD] *[a] Na Liu[a] and Li Wei[a]

Seaweed residue (SR) is an industrial by-product produced during seaweed extraction, which is generally used in feed processing with low added value and cheap price (<0.2 $ per kg). In this study, we reported that Nano Seaweed residue fibers were extracted from seaweed residue, and SR-CNF was prepared by pretreatment of SR with oxalic acid (OA) dihydrate combined with an assisted ultrasonic disintegration method. The effects of different OA contents on the yield and physicochemical properties of SR-CNF, as well as the potential value of the application of seaweed residue-based biocomposite films were investigated in the pretreatment system. It has some reference value for the exploration of algal residue-based nanofiber preparation. Using the casting method, the SR-CNF was used as the reinforcing material, and the algal residue-based composite film was prepared with an elongation at break of 83.2% and a tensile strength of 12.9 MPa. The film has good light transmittance, and it also possesses moderate tensile strength as well as excellent UV protection. Of particular interest is that this UV shielding effect is entirely derived from the natural color-emitting groups within the material, a unique property that makes the composite film have great application prospects in the field of food packaging.

1 Introduction

Cellulose nanofibrils (CNFs) represent a distinct form of nanocellulose characterized by their nanoscale diameters and lengths that can range from nanometers to micrometers. With the advancement of nanoscience and technology, CNFs have garnered increasing global attention for their industrial applications. Owing to their biocompatibility, biodegradability, high surface area, high reactivity, and superior mechanical properties, CNFs exhibit significant potential across various sectors, including textiles, paper, coatings, packaging, pharmaceuticals, and water treatment, among others.[1]

CNFs can be isolated and prepared from raw cellulose materials through mechanical treatments such as fine grinding, high-pressure homogenization, or ultrasonication, or through a combination of chemical pretreatment and mechanical processing.[2] However, to achieve large-scale production and commercial utilization, researchers face significant challenges in producing CNFs with high yield and high quality in an environmentally friendly and economically viable manner.[3]

In this context, numerous studies have been conducted to reduce the production costs and environmental impact of CNFs. Utilizing low-cost cellulose sources as raw materials is one of the effective strategies to lower the cost of CNF production. Terrestrial plants, algae, and fungi are rich in cellulose content. Therefore, lignocellulosic biomass, such as agricultural or woody waste, is commonly used as a low-cost cellulose raw material for CNF preparation, instead of more expensive options like pulp or cotton fibers. CNFs have been successfully prepared from various sources, including sugarcane,[4] pineapple residue,[5] straw,[6] peanut shells,[7] coconut shells,[8] and corn stalks.[9] However, the removal of lignin remains a significant challenge in extracting cellulose from lignocellulosic biomass. Harsh chemical treatments of biomass can partially degrade cellulose and generate effluents with severe environmental concerns.[10] Additionally, the collection and transportation of agricultural and woody wastes can be challenging, potentially increasing the cost of raw materials.[11] Given the rapidly growing demand for cellulose and its derivatives, it is crucial to identify additional sources of cellulose.[12]

Therefore, easily available and fast-growing algae biomass, such as seaweed, is gaining global attention as an additional cellulose source for the preparation of CNFs.[13] Liu *et al.*[14] prepared CNFs from sargasso using a 7% (v/v) hydrochloric acid aqueous solution followed by ultrasonic treatment. The sargasso CNFs, characterized by their extremely long length (15–20 μm) and natural nanostructure, show promise as

[a]*School of Light Industry and Chemical Engineering, Dalian Polytechnic University, Dalian 116034, China. E-mail: shaoguolin@dlpu.edu.cn; Tel: +86 0411 86323726*

[b]*Wuxi Zhongwei Knowledge Integration Co., Ltd, Wuxi 214001, China*

[c]*Dalian Zhonghuida Scientific Instrument Co. Ltd, Dalian 116023, China*

† These two authors contributed equally to this paper.

reinforcement materials. Composite films prepared with chemically cross-linked sargasso CNFs and polyvinyl alcohol (PVA) exhibited outstanding water resistance and mechanical performance. Salem and Ismail[15] investigated the isolation and characterization of cellulose and CNFs from six seaweed species collected from the Mediterranean coast (Egypt). The CNFs were prepared from crude seaweed cellulose *via* acid hydrolysis, with yields ranging from 9.1% to 47.7%, shapes varying from filaments to plates, and average sizes ranging from 14.94 to 30.82 nm, depending on the seaweed species. These selected seaweeds can serve as a renewable source of CNFs with economic applications. Furthermore, seaweed CNFs exhibit significantly higher crystallinity, smaller diameters, and better thermal stability compared to CNFs derived from lignocellulosic biomass.

Currently, seaweed is primarily processed to extract phycolloids, which are the major known constituents of biomass. Annually, 594 200 dry tons of seaweed are used globally to produce carrageenan, agar, and alginate in the phycolloid industry. The residual biomass left after the extraction of phycolloids, referred to as seaweed residue (SR), is typically treated as waste or used as animal fodder. SR is particularly rich in cellulose, with a content of over 42%. Processing SR for the production of cellulose or its derivatives can help transform waste into valuable materials. Specifically, the preparation of CNFs from SR offers an opportunity for large-scale extraction and utilization of cellulose for various applications.

There have been two notable reports on the successful preparation of cellulose nanocrystals (CNCs), a type of nanocellulose, from SR. Liu *et al.*[16] prepared CNCs from industrial kelp waste with a yield of 52.3% and a crystallinity index (CrI) of 69.4%. Achaby *et al.*[17] used red seaweed waste to produce high-quality CNCs with diameters of 5.2–9.1 nm and lengths of 295.4–315.7 nm, and a CrI of 81–87%, which varied with the hydrolysis time (30–80 minutes). The resulting CNCs can be used as reinforcing fillers to enhance the mechanical properties of PVA-based composite films.

For CNFs, another type of nanocellulose, Dai *et al.*[18] successfully prepared 2,2,6,6-tetramethylpiperidine-1-oxyl (TEMPO) oxidized CNFs from SR, which can be used as the framework for cellulose aerogels for oil/water separation. Generally, the production of CNFs from SR has been less reported compared to CNCs. It is noteworthy that, in all the abovementioned works about the CNF production from seaweed or SR, the bleaching treatment was carried out to eliminating the pigment. The chemical agents used in the bleaching treatment, *i.e.* $NaClO_2$ or H_2O_2, has some dangerous characteristics, for example: poisonous, explosive, and so on. If there were not the specific needs to apparent color or transparency, the bleaching treatment might not be required. In addition, the bleaching could lead to the decrease of yield and change of crystalline structure of CNF. However, to the best of our knowledge, there has rarely about the CNF production from SR without bleaching so far.

In this study, CNFs were produced from SR using pretreatment with an oxalic acid (OA) aqueous solution followed by high-intensity ultrasonic disintegration, without bleaching treatment. This product is referred to as SR-CNF. The effects of OA concentration on the yield and physicochemical properties of SR-CNF were comprehensively investigated. PVA-based composite films were prepared using SR-CNF as the reinforcing agent, and their ultraviolet shielding and mechanical properties were thoroughly evaluated.

2 Materials and methods

2.1 Materials

The 40-mesh dried SR was supplied by Qingdao Haixinyuan Biotechnology Co., Ltd (China). According to the analytical procedures (GB/T 5009.10-2003, GB 5009.4-2016, GB/T 14772-2008, GB/T 5750.4-2006, Chinese standard methods), the contents of cellulose, ash, lipids, and water-soluble substances were 65.0%, 24.7%, 3.9%, and 6.4% by weight, respectively, on a dry basis (unless otherwise stated), as tabled in Table S1 in SI. The SR was repeatedly washed with deionized (DI) water until the supernatant became almost transparent. The washed SR was then dried at 105 °C until a constant weight was achieved and stored in a desiccator for subsequent use.

The commercial CNFs (CM-CNFs) were purchased from Jinan Shengquan Group Shareholding Co., Ltd PVA (M_n: 16 000 g mol^{-1}), sodium carboxymethyl cellulose (CMC, DS = 0.7), glycerol (≥99.0%), oxalic acid dihydrate (≥99.0%), and anhydrous ethanol (≥99.0%) were obtained from Shanghai Aladdin Biochemical Technology Co., Ltd. All chemical reagents were used without further purification. Deionized (DI) water with a conductivity of 0.057 μS cm^{-1} was used in this study.

2.2 Preparation of SR-CNFs

The SR was first pretreated using OA solutions with varying concentrations (10–60%). Two grams of SR were added to a 250 mL round-bottomed flask containing 160 g of the OA solution, and the mixture was continuously stirred at 110 °C for 3 hours. The pretreated SR was then repeatedly washed until the washing liquid reached a neutral pH.

Ultrasonic disintegration was performed using an ultrasonic cell crusher equipped with a 25 mm diameter cylindrical titanium alloy amplitude horn (JY99-IIDN, Shanghai Huanalysis Industry Co., Ltd). The pretreated SR was dispersed in deionized (DI) water at a concentration of 0.4%. The ultrasonic treatment parameters were set as follows: treatment time of 15 minutes, output power of 1000 W, and frequency of 20 kHz. The resulting suspension was allowed to stand for 72 hours, after which the supernatant was collected by removing the precipitated residues at the bottom. The SR-CNF sample was obtained by lyophilization for further characterization.

The yield of SR-CNF was calculated using the following equation:[19]

$$\text{CNF yield (\%)} = \frac{V_1(m_1 - m_2)}{M \times V_2} \times 100\%　\qquad (1)$$

where M represents the mass of the raw material in grams, m_1 is the combined weight of the vessel and the transferred suspension after drying in grams, m_2 is the mass of the vessel in grams,

V_2 indicates the volume of the transferred suspension in milliliters, and V_1 is the total volume of the suspension in milliliters. The error values were calculated after three repetitions of each reaction. For the sake of simplification, SR-CNF prepared by pretreatment with a certain concentration (XX%) of OA solution is designated as SR-CNFXX. For example, SR-CNF60 refers to SR-CNF prepared by pretreatment with a 60% OA solution.

2.3 Preparation of composite films

The typical composite film was prepared using the following procedure. A 50 mL CMC solution (2.5%) was mixed with a 50 mL PVA solution (5%) at 60 °C to obtain a homogeneous solution. Subsequently, a specific amount of glycerol (1.25%, v/v, based on the total volume of the PVA-CMC solution) was added to the mixture under continuous mechanical stirring until a homogeneous film-forming solution was achieved. The resulting PVA/CMC/glycerol solution was used to prepare the composite film (abbreviated as PMG) by the casting method. The film solution (20 mL) was poured into a 6 cm diameter polystyrene mold and dried at 45 °C for 48 hours to ensure complete drying. The prepared composite film (PMG) was then removed from the mold.

Three additional types of mixed solutions for film casting were prepared following the same procedure, with the only difference being the type of reinforcing agent added to the CMC solution. Specifically, 50 mL of CMC solution was mixed with a specific amount of CM-CNF, SR-CNF20, or SR-CNF60 to achieve a final CNF content of 1.25 wt%. Thus, the three types of composite films, namely PVA/CMC/glycerol/CM-CNF (PCG), PVA/CMC/glycerol/SR-CNF20 (PNG20), and PVA/CMC/glycerol/SR-CNF60 (PNG60), were prepared accordingly.

2.4 Characterization of SR-CNF

2.4.1 Scanning electronic microscope (SEM). A 0.1% (w/v) suspension of SR-CNF was applied onto a copper grid coated with carbon conductive adhesive and treated with a gold spray. The microstructure of the SR-CNF was examined using a thermal field emission SEM (JSM-7800F, Nippon Electron Co., Ltd, Japan) at a low acceleration voltage of 5 kV. One hundred samples were randomly selected from the SEM images of each SR-CNF, and their dimensions (length and diameter) were measured using Nano Measure 1.2 software. The size distributions of the prepared SR-CNFs were then determined statistically.

2.4.2 Fourier transform infrared spectroscopy (FT-IR). The functional group changes of SR-CNF were investigated using a Spectrum Two FT-IR spectrometer (PerkinElmer, USA). The infrared scanning wavenumber range was 400–4000 cm^{-1}, with a resolution of 4 cm^{-1} and 16 scans.

2.4.3 X-ray diffraction (XRD). The crystal structures of the prepared SR-CNF samples were characterized using a Shimadzu XRD-6100 diffractometer, operated at a scanning rate of 5° min^{-1} over a diffraction angle range of 5° to 40°. The instrument was operated at a voltage of 40 kV and a current of 20 mA. The relative crystallinity index of the samples was determined using the Segal method.[20]

$$\mathrm{CrI}\,(\%) = \frac{I_{002} - I_{\mathrm{am}}}{I_{002}} \times 100\% \qquad (2)$$

where I_{002} represents the crystallinity at $2\theta = 22.6°$, while I_{am} denotes the crystallinity at $2\theta = 18°$. The crystallite spacing (d) was calculated by the (Braggs) method.[19]

$$n\lambda = 2d \sin \theta \qquad (3)$$

Grain size D_{hkl} of the samples was obtained with the following formula (Scherrer method).[21]

$$D_{hkl} = \frac{k\lambda}{F_{\mathrm{w}} \times \cos\theta} \times 100\% \qquad (4)$$

where k represents Scherrer's constant, which is assumed to be 0.943, λ corresponds to the X-ray wavelength, assumed to be 0.154 nm, and F_{w} denotes the maximum half-height width of the related characteristic diffraction peak.

The Z value was calculated using the following formula.[22]

$$Z = 1693d_1 - 902d_2 - 549 \qquad (5)$$

2.4.4 Thermogravimetric analysis (TGA). The thermal properties of SR-CNF were measured using a Q500 TG analyzer (TA Instruments, USA). A sample weighing 5 mg was heated from 30 °C to 600 °C at a heating rate of 10 °C min^{-1}, with high-purity nitrogen used as the carrier gas at a flow rate of 25 mL min^{-1}.

2.4.5 Zeta potential and hydrodynamic size. The SR-CNF suspension was diluted to 0.01% and homogenized using ultrasound for 10 minutes. The zeta potential of the SR-CNF was subsequently measured using electrophoretic light scattering (Nano ZS, Malvern, UK). The hydrodynamic size of the SR-CNF was determined using dynamic light scattering (DLS), and the refractive indices of SR-CNF and water were set to 1.47 and 1.33, respectively.

2.4.6 UV-vis spectroscopy. The UV-vis transmission spectra of 0.1% CNF suspensions in DI water were analyzed using a 722SP spectrophotometer (Nippon Electronics Corporation Co. Ltd, Japan) over the wavelength range of 200 to 800 nm. DI water was used as the blank.

2.5 Characterization of composite films

2.5.1 Mechanical properties. Mechanical strength was assessed with an electronic universal materials testing instrument (Instron 5965, Boston Instron Co. Ltd, USA). The composite films were prepared and cut into strips measuring 80 mm × 20 mm (length × width). The distance between the two fixtures was 40 mm, with a tensile rate of 10 mm min^{-1}. The tensile stress–strain curves were then averaged over five measurements.

2.5.2 UV-vis spectroscopy. The optical properties of prepared composite films were analyzed through employment of a dual-beam UV-vis is spectrophotometer (Nippon Electronics Corporation Co. Ltd, Japan). To ensure accuracy, five measurements were taken and the transmittance was calculated as an average.

2.5.3 Morphology. The morphology and microstructure analysis of the presently prepared composite films was executed through the utilization of scanning electron microscopy (SEM) under an accelerating voltage of 5 kV, using JSM-7800F, JEOL from Japan. The synthesized PVA/CMC/CNF hybrid films became fragile and ruptured when exposed to liquid nitrogen.

3 Results and analysis

3.1 Yield and component analysis of SR-CNFs

To fabricate high-quality SR-CNF, an OA–water pretreatment was employed in conjunction with ultrasonic disintegration, and a thorough investigation into the impact of OA concentration on the yield of SR-CNF was conducted. Observations from Fig. S1 in SI reveal that as the concentration of OA increases, the color of the SR-CNF suspensions and their corresponding dried samples progressively lightens. This phenomenon is likely attributable to incomplete acid hydrolysis at lower OA concentrations, whereas the H^+ ions in higher concentrations of OA can effectively penetrate the amorphous regions of cellulose, achieving deep decolorization by converting chromophoric groups to colorless ones. As indicated in Table 1, further research has demonstrated that under the pretreatment condition of 20% OA, the yield of SR-CNF reaches its peak value of 57.3%. This finding elucidates the optimal balance between OA concentration and SR-CNF yield. With further increases in OA concentration, there is no significant enhancement in SR-CNF yield, which may be attributed to excessive hydrolysis induced by high concentrations of OA. This is consistent with the findings of Mite et al.[23] during the isolation of nanocellulose from cocoa bean husks. Nanocellulose is obtained through the breakdown of the macroscopic cellulose fiber structure, where the amorphous regions with disordered glucose chain distribution are more susceptible to hydrolysis, while the crystalline regions exhibit greater resistance to hydrolysis. The removal of amorphous regions near defect sites of microfibrils results in the formation of nanocellulose. High concentrations of OA can lead to the chemical degradation of cellulose, converting it into simpler molecules such as glucose and other polysaccharides.[24]

Compositional analysis of SR (Table S1) revealed that it is primarily composed of cellulose (64.74%) and a significant proportion of ash (24.43%). The ashes are primarily composed of elements (Fig. S2) such as calcium (Ca), potassium (K) and

silicon (Si). Regarding ash content, Table 1 indicates that SR-CNF obtained from lower concentrations of OA (10–30%) pretreatment has a lower ash content (4.2%), while the corresponding residues have a higher ash content (8.5%). As the concentration of OA increases, the ash content in SR-CNF initially increases and then decreases, whereas the ash content in the residues initially decreases and then increases. This phenomenon may be attributed to the fact that high concentrations of OA not only degrade the amorphous regions of cellulose but also affect the crystalline regions, leading to the chemical degradation of cellulose.[25]

The findings of this study provide valuable insights for the efficient production of SR-CNF, particularly regarding the selection of OA concentration in the pretreatment. By precisely controlling the OA concentration, the yield and quality of SR-CNF were enhanced while simultaneously reducing the ash content. This is of paramount importance for enhancing the application value of SR-CNF in both industrial and research contexts.

3.2 Characterization of SR-CNFs

3.2.1 SEM. SEM was used to analyze the micromorphology of SR-CNF obtained with OA–water pretreatments of different OA concentrations. The results are presented in Fig. 1 and S3, which clearly demonstrate that all SR-CNF samples exhibit good dispersibility and a slender fiber structure. The samples prepared with 60% OA exhibit smaller dimensions and a more uniform diameter distribution. According to the observations, the pretreatment and ultrasonic steps weaken the intermolecular hydrogen bonding within the SR cellulose, leading to the cleavage of glycosidic bonds and the formation of nanoscale fiber structures.[26,27] The length and diameter distribution of SR-CNF were measured and are depicted in Table S2. During the chemical pretreatment process, as the concentration of OA increases, the average length and aspect ratio of SR-CNF decrease. When the OA concentration is increased from 10% to 60%, the average diameter of individual fibers decreases from 36.0 nm to 21.4 nm, and the average length shortens from 957.6 nm to 419.7 nm. This suggests that high concentrations of OA can effectively sever the cellulose molecular chains and disrupt the hydrogen bond network between the cellulose nanofibers. The concentration of OA in the pretreatment solvent is one of the critical factors for enhancing the quality and performance of SR-CNF.

3.2.2 FT-IR analysis. The FTIR analysis presented in Fig. 2a reveals the chemical structure of SR-CNF extracted from SR. The stability of the chemical structure of SR-CNF after treatment with aqueous OA solution was also confirmed. The peak at 3350 cm^{-1} corresponds to the stretching vibrations of O–H groups, which facilitate the formation of intramolecular and intermolecular hydrogen bonds. Additionally, the enhanced characteristic peaks of stretching vibrations indicate that SR-CNF possesses strong hydrophilicity.[28] The peak at 2920 cm^{-1} is attributed to the stretching vibrations of C–H groups.[29] The peak at 1734 cm^{-1} corresponds to the stretching vibrations of the carbonyl group C=O, indicating that an esterification reaction has occurred between OA and cellulose, forming

Table 1 Yield of SR-CNFs and ash content in samples

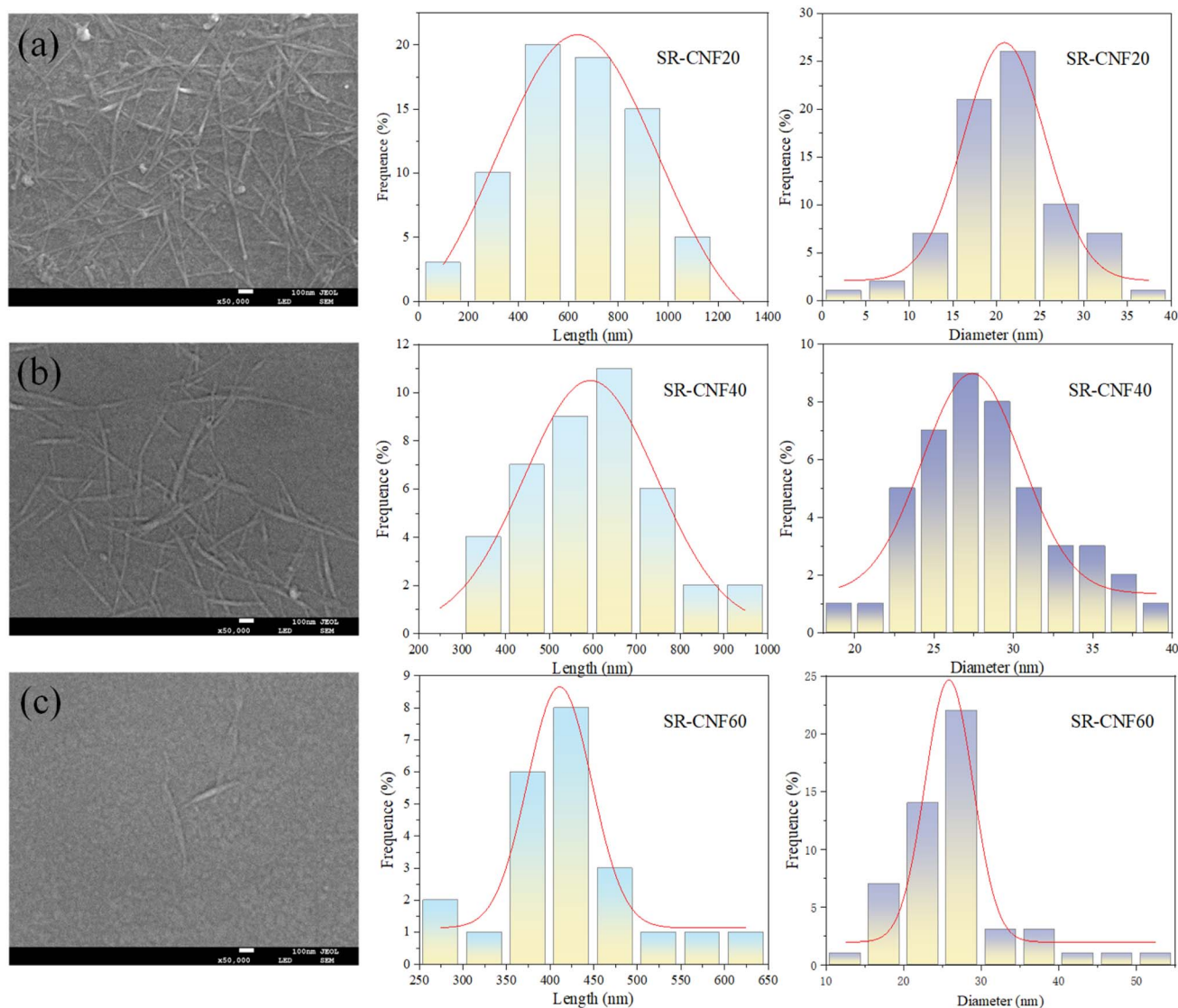| OA concentration (%)	SR-CNF yield (%)	Ash content	
		SR-CNFs (%)	Residues (%)
10	46.2 ± 1.0	4.2 ± 0.5	8.5 ± 1.2
20	57.3 ± 1.2	5.4 ± 0.8	7.0 ± 1.4
30	52.2 ± 1.8	9.8 ± 1.9	2.8 ± 0.6
40	32.9 ± 1.1	10.8 ± 1.4	1.9 ± 0.4
50	30.8 ± 1.9	8.8 ± 2.3	3.3 ± 0.8
60	25.9 ± 1.6	5.2 ± 1.2	7.3 ± 0.3

Fig. 1 SEM images of SR-CNFs prepared with OA–water pretreatments. SR-CNF20 (a), SR-CNF40 (b), and SR-CNF60 (c).

covalent bonds. These ester bonds are likely located on the C6 position of cellulose.[30] The esterification reaction between the C2, C3, and C6 positions of cellulose and OA is a rapid process. High concentrations of OA not only act as a catalyst for cellulose hydrolysis but also serve as a reaction substrate and solvent medium, enhancing the degree of esterification between OA and cellulose. This explains why esterification reactions are less pronounced at low concentrations of OA.[31] The peak at 1627 cm^{-1} is attributed to the formation of carboxylate esters, indicating the interaction between water and cellulose that leads to the bending of water molecules, potentially involving the presence of carboxyl and hemiacetal groups. The peak at 1428 cm^{-1} represents the intermolecular hydrogen bonding of the C6 group in cellulose, signifying the bending vibrations of the cellulose I structure. The peak at 1322 cm^{-1} corresponds to the symmetric stretching vibration of C–H groups. Furthermore, the peak at 1060 cm^{-1} is associated with the vibrational absorption of the reducing end carbon C1 in cellulose, revealing

the stretching vibrations of β-glycosidic bonds and O–C–O, while also indicating the presence of amorphous cellulose.[32]

3.2.3 XRD analysis. As depicted in Fig. 2b, the XRD patterns of SR-CNF treated with varying concentrations of OA reveal two prominent diffraction peaks located at approximately 14.9° and 22.7°, respectively. The presence of these peaks confirms the I$_\alpha$ and I$_\beta$ cellulose crystal structures characteristic of cellulose I. After the pretreatment process involving acid and ultrasonic disintegration, no significant changes in the crystal structure are observed, indicating the preservation of the native crystallinity throughout the preparation process.

As shown in Table S3, the crystallinity index (CrI) of the prepared SR-CNF samples (ranging from 62.50% to 71.47%) was generally lower than that of the SR sample (76.73%). This reduction can be attributed to the disruption of the crystalline region caused by the OA–water pretreatment and the ultrasonic disintegration process. As the concentration of OA increased from 10% to 60%, the CrI initially increased and then
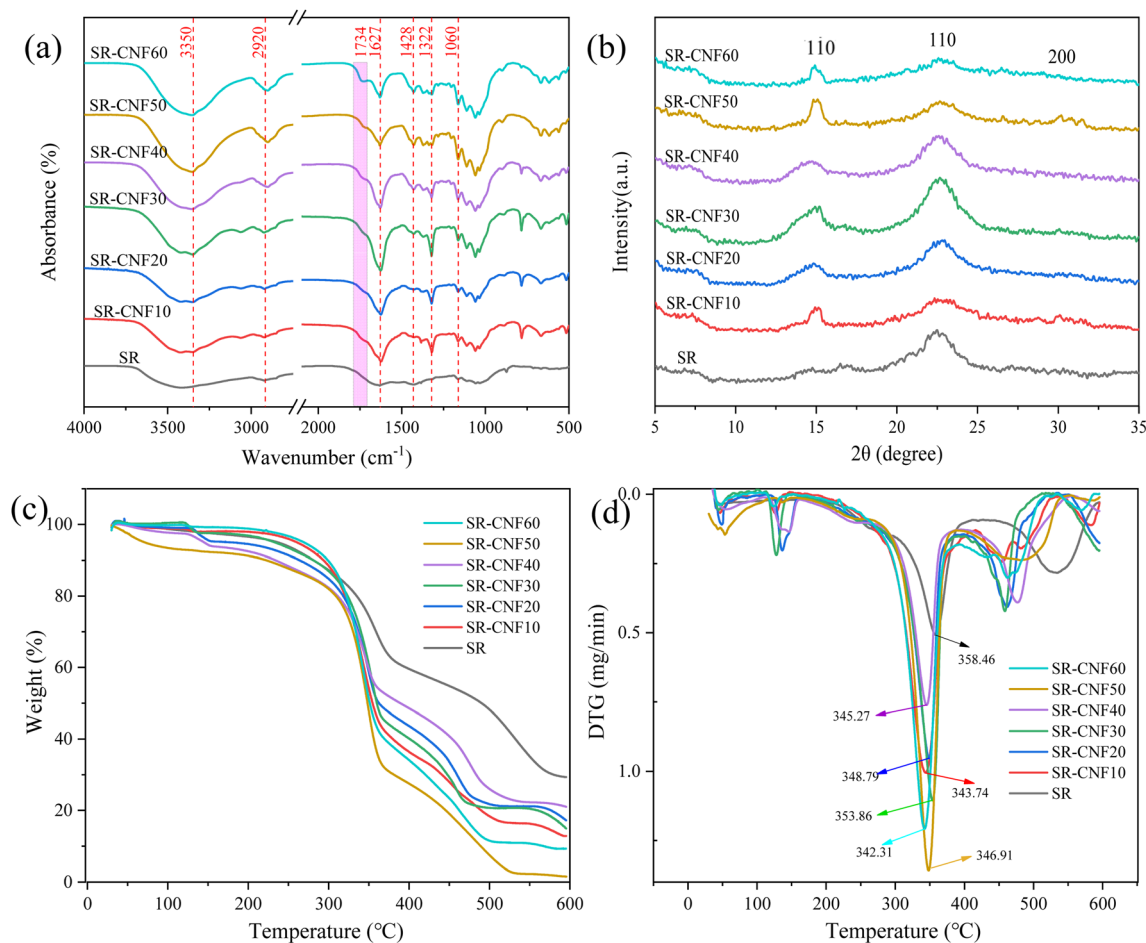
Fig. 2 FTIR spectra (a), XRD patterns (b), TG (c) and DTG (d) curves of SR and prepared SR-CNFs.

subsequently decreased. This trend may be explained by the degradation of the amorphous regions of cellulose during the hydrolysis process. Notably, the SR-CNF prepared with 30% OA exhibited the highest degree of crystallinity, with a CrI of 71.47%. This value is higher than the crystallinity reported by Liu *et al.*[16] for CNC prepared from kelp waste, which had a crystallinity of 69.4%. The lower crystallinity could be due to the bleaching and alkali treatments applied before pretreatment, which disrupt the amorphous or paracrystalline regions of cellulose, leading to the hydrolysis of β-1,4-glycosidic bonds and the release of individual crystalline segments.[33,34]

The peak near 22° indicates the presence of the 200 crystal plane within the crystalline regions, ensuring the integrity of the cellulose crystalline structure. Meanwhile, the peak near 14° represents the amorphous region, which contains the $1\bar{1}0$ (14.8°) and 110 (16.5°) crystal planes. The stable existence of these planes guarantees the integrity of the cellulose I structure. In the cellulose I structure, both I_α and I_β crystals coexist, representing monoclinic and orthorhombic unit cells, respectively. The I_β crystal is more stable than the I_α crystal.[35] The interplanar spacing, denoted as d, is commonly used to analyze the variations between the types of cellulose (I_α and I_β). The Z-value, a crystal structure determination factor, indicates the

predominant cellulose structure when $Z > 0$. The interplanar distances d_1, d_2, and d_3 correspond to the spacings of the $1\bar{1}0$, 110, and 200 crystal planes, respectively. Changes in the d-values also reflect shifts in the positions of the diffraction peaks.[36] Investigating the crystal grain size D_{hkl} provides further insights into the variations in the crystallinity of SR-CNF.

The detailed data obtained from the XRD analyses are presented in Table S3. The variation in the $1\bar{1}0$ crystal plane is not significant, while changes in the 110 crystal plane reflect the distinct impacts of pretreatment and ultrasonication on each crystal plane. Overall, as the OA concentration increases from 10% to 60%, D_{hkl} increases from 8.7 to 12.8, but the CrI does not correspondingly increase. This may be due to H^+ penetration into both the crystalline and amorphous regions of cellulose, leading to the release of individual crystalline segments.[37] The D_{hkl} of the 200 crystal plane in SR-CNF is enhanced compared to the raw material SR, increasing from 3.33 nm to 3.59–4.47 nm, and the D_{hkl} of the 110 crystal plane increases from 8.70 nm to 8.29–12.84 nm. This may be attributed to the higher content of O–H groups in the 110 crystal plane at increased OA concentrations, making it more susceptible to hydrolysis.[38] The chemical pretreatment-ultrasonic disintegration method promotes the disassembly of the amorphous regions of

cellulose and enhances the orderliness of the crystalline regions, resulting in changes in D_{hkl}. This trend is consistent with that of CrI, reflected in the increase of D_{hkl} for the $1\bar{1}0$, 110, and 200 crystal planes. This indicates that the preparation process of SR-CNF does not alter the crystal structure of cellulose but modifies its CrI and D_{hkl}. This is attributed to the breaking and reformation of hydrogen bonds along the cellulose chains, with the amorphous region hydrogen bonds being more easily disrupted, leading to a reduction in the amorphous region and a relative increase in the crystalline region of SR-CNF. Consequently, this results in an increased CrI for SR-CNF prepared with 30% OA.[39]

3.2.4 Thermogravimetric analysis. Thermal stability is a critical parameter for the application of nanocellulose and is essential for enhancing the performance of reinforcing materials. Fig. 2c and d illustrate the thermal degradation properties of SR-CNF prepared with pretreatment using various concentrations of OA, with the corresponding data summarized in Table S4. Compared to the raw SR, SR-CNF pretreated with OA–water exhibited reduced thermal stability, primarily due to the significant impact of acid hydrolysis on the amorphous regions. During the OA–water pretreatment of SR, the removal of amorphous materials and ash, as well as the destruction of some crystalline components, occurred.[40] The changes observed in the degradation curves during the OA–water pretreatment of SR can be attributed to the chemical reactions of OA groups on the cellulose surface. The introduction of carboxylic groups tends to decrease the thermal stability of the SR-CNF product.[41]

Fig. 2c and d clearly depict the three degradation stages experienced by SR-CNF prepared at different OA concentrations (10–60%). The presence of cellulose leads to thermal decomposition within a specific temperature range, characterized by several distinct degradation peaks. Notably, SR-CNF obtained through pretreatment with 30% OA exhibited enhanced thermal stability, with the maximum thermal decomposition temperature (T_{max}) reaching 353.7 °C. Materials with high thermal stability typically possess a high CrI value, as corroborated by the XRD data (Table S3), and surpass the T_{max} of nanocellulose extracted from pineapple waste by Neenu et al.[42] (336 °C). This is a significant advantage for applications requiring high-temperature processing, such as thermoforming. However, SR-CNF prepared using higher concentrations of OA (40–60%) pretreatment did not demonstrate superior thermal stability, which may be attributed to the partial destruction of the crystalline regions during acid hydrolysis.

Within the temperature range of 30–110 °C, the weight loss is primarily attributed to the evaporation of free water within the fibers, further confirming the hydrophilic characteristics observed at 1627 cm^{-1} in the FT-IR spectra (Fig. 2a). Additionally, volatile impurities are also decomposed at these lower temperatures.[43] The degradation peak at 340–350 °C corresponds to the main DTG peak, involving partial dehydration, dehydroxylation, disintegration, and glycosidic bond cleavage of cellulose.[44] All SR-CNF samples exhibit a degradation peak beyond 450 °C, indicating the ultimate decomposition of cellulose into carbon and other products. At 600 °C, the TGA shows a relatively high residual content for the raw SR (29.4%),

attributed to its high ash content of 24.4%. The ash content of SR-CNF prepared through OA–water pretreatment shows a decreasing trend, with the char residue at 500 °C decreasing from 21.0% to 8.5% as the concentration of OA increases (Table 1). This is consistent with the carbon residual data of CNC extracted from industrial kelp by Liu et al.[16]

3.2.5 Dynamic light scattering and zeta potential analysis. Carboxylation treatment effectively increases the surface charge of fibers, which is crucial for the application of nanofiber materials. Following ultrasonic disintegration of SR, the degree of fiber disintegration is enhanced, ultimately leading to the formation of a stable SR-CNF suspension. Zeta potential measurements provided data on the surface charge of SR-CNF. As shown in Fig. S4, the zeta potential of SR-CNF suspensions ranged from −22 to −32 mV, indicating consistently negative values that provide a solid foundation for the stability and transparency of SR-CNF suspensions. Higher zeta potential values indicate stronger electrostatic repulsion between nanofibers, resulting in improved dispersion and preventing aggregation in the suspension.[45,46] OA, as a weak acid, can induce the formation of negatively charged carboxyl groups on the cellulose surface.[47]

The DLS profiles in Fig. 3 reveal that the average hydrodynamic size of SR-CNF ranges from 5 to 600 nm, with varying concentrations of OA pretreatment significantly impacting the average hydrodynamic size of SR-CNF. As the concentration of OA increased from 10% to 60%, the number of non-disintegrated fiber aggregates decreased, and the electrostatic repulsion between fibers significantly increased (from −22 to −32 mV), with the hydrodynamic size gradually concentrating within the 100 nm range from an initial 600 nm. Notably, these results differ from those reported by Henschen et al.,[48] who suggested that the amount of OA had a limited effect on the size distribution of CNF. This discrepancy may be attributed to the varying degree of destruction of cellulose microfibers during the acid hydrolysis of SR with OA–water.[49] At low concentrations of OA (10–30%), the acidolysis capacity for cellulose microfibers is relatively weak, resulting in larger hydrodynamic sizes measured by DLS. In contrast, at higher concentrations of OA (40–60%), combined with the effects of ultrasonic
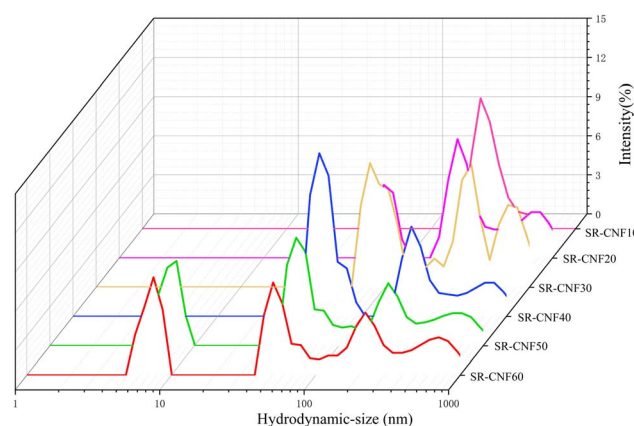

Fig. 3 DLS measurement of suspensions.

disintegration, the acidolysis process of cellulose microfibers is accelerated, enabling faster destruction of cellulose fibers and controlling the average hydrodynamic size within 100 nm.

3.2.6 UV-vis spectroscopy observation.

Observations from Fig. 4 indicate a gradual increase in the light transmittance of SR-CNF suspensions with increasing OA concentration. According to the data presented in Table 2, the SR-CNF10 suspension, which was pretreated with 10% OA, achieved a UV-blocking rate of 93.2% in the long-wave UV region and an even more impressive 96.2% in the middle-wave UV region. In contrast, the SR-CNF60 suspension, prepared using 60% OA, exhibited a UV-blocking rate of 54.5% in the long-wave UV region and 71.6% in the middle-wave UV region. These findings reveal a significant impact of OA concentration on the UV-blocking properties of SR-CNF. This finding differs from the observations made by Neenu et al.,[5] who used OA and sulfuric acids as solvents for extracting nanocellulose from pineapple waste and reported minimal impact of OA concentration on UV transmittance. The findings indicate that higher concentrations of acid effectively reduce the dimensions of cellulose, thereby enhancing the UV light transmittance. On the contrary, it reduces UV blocking capabilities.

Such discrepancies may stem from the high content of silicates and other inorganic ash components present in SR. Under low concentrations of oxalic acid, a portion of H^+ may react with the ash, whereas at higher acid concentrations, a greater amount of H^+ interacts with cellulose chains and glycosidic bonds. Nanocellulose solutions with high transmittance rates imply a stronger charge effect, which aligns with the zeta potential of SR-CNF solutions, as shown in Fig. S4, ranging from −22 to −32 mV and all being negative. Notably, the SR-CNF60 suspension at a 0.05 wt% concentration exhibits a charge of −32 mV. Such highly charged SR-CNF solutions demonstrate uniform dispersion and enhanced light transmittance, attributed to the hydroxyl oxidation effect that generates hydrophilic carbonyl groups. This is consistent with the esterification observed in the infrared spectroscopy, where OA reacts with SR-CNF to form carbonyl C=O stretching vibrations on the C_6 position of cellulose.

3.3 Characterization of composite films

3.3.1 Optical properties of composite films.

During the drying process, nanocellulose self-assembles into a network, thereby forming a uniform thin film. SR-based composite films were prepared using the casting method, specifically PNG20, PNG60, PMG, and PCG, as shown in Fig. 5a. All films had a thickness of approximately 0.20 mm. Films prepared using commercially available nanocellulose (PCG) and carboxymethyl cellulose (PMG) exhibited higher transparency, while composite films prepared from unbleached SR-CNF solutions also demonstrated a certain level of light transmittance. The color of SR-CNF20 was darker than that of SR-CNF60, primarily due to insufficient acid hydrolysis at low concentrations of OA. In contrast, the H^+ ions in high concentrations of OA can penetrate the amorphous regions, leading to the bleaching of cellulose.[50] This is consistent with the color observed after the dried SR-CNF (Fig. S1b).

The UV-visible spectra of the composite films are depicted in Fig. 5b. According to the data in Table S5, PNG20 exhibits UV-blocking rates of 95.8% and 98.7% for the UVA and UVB wavelength ranges, respectively, demonstrating superior UV shielding effects compared to PMG and PCG. As clearly observed in Fig. 5c, among the four different films under UV exposure, the blank group without film coverage reveals the number "0" distinctly, while samples covered with PMG and PCG allow for a faint discernment of the number "0". In contrast, samples covered with PNG20 and PNG60 completely obscure the number "0", indicating that the incorporation of SR-CNF significantly enhances the UV-blocking capability of the films 30. This shielding is primarily attributed to certain chromophoric groups present in the SR, which effectively absorb UV radiation. Upon scrutinizing the FTIR data of SR in Fig. S5, the absorption of the C=O appeared at 1642 cm^{-1}. Two additional strong absorptions of SR at 3420 and 1068 cm^{-1} are assigned to the O–H and C–O sugar groups of these glycosyl esters. They can absorb UV light in the UV-A and some UV-B bands and efficiently burst excited-state single-linear oxygen and free radicals.
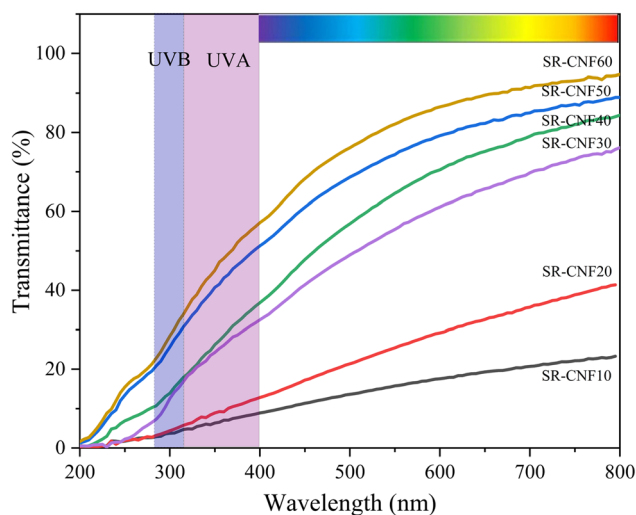

Fig. 4 UV-Visible transmittance of SR-CNF.

Table 2 UVA and UVB blocking rates of 10–60% different concentrations acid-treated SR[a]

	SR-CNF10	SR-CNF20	SR-CNF30	SR-CNF40	SR-CNF50	SR-CNF60
$B_{UV-A\%}$	93.2	90.7	75.3	72.6	59	54.5
$B_{UV-B\%}$	96.2	95.5	87.9	85.7	74.2	71.6

[a] Where, $B_{UV-A\%}$ represents the blocking rate in the long-wave UV region, while $B_{UV-B\%}$ represents the blocking rate in the medium-wave UV region.
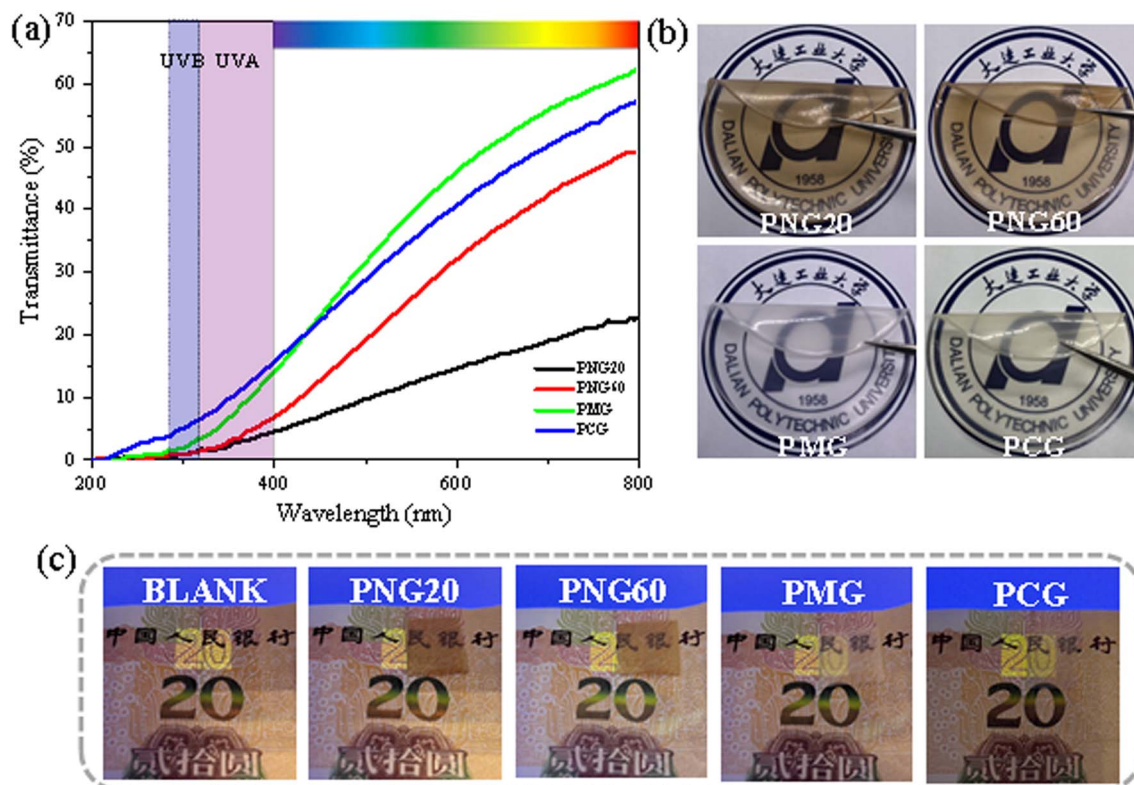
Fig. 5 UV shielding performance (a), optical transparency (b), and UV blocking ability (c) of the prepared composite film.

The absorption peak at hand is primarily linked to the stretching vibration of the C–H bond at 2850 cm^{-1}, specifically corresponding to the vibrational mode of the long-chain alkyl group. This mechanism is similar to the UV-blocking properties of the antioxidant films prepared by Pascual et al.[51] from Sargasso, where the presence of functional groups, contribute to the obstruction of UV middle and long wavelengths. The findings indicate that composite biofilms based on SR possess significant potential for UV-blocking applications.

SEM images, as presented in Fig. S6, illustrate the surface morphology of the films. It can be observed that the film surfaces are not entirely smooth but exhibit some protrusions. Notably, Fig. S6(a) shows a higher number of these protrusions compared to Fig. S6(b), primarily due to the presence of ash content. This surface morphology bears similarities to the nanocellulose films produced using quinoa and starch by Safar et al.[52] Overall, the composite biofilms prepared from SR demonstrate satisfactory transparency and UV resistance, highlighting their potential for applications in the packaging industry.

3.3.2 Mechanical properties of composite biofilms.

Tensile strength and elongation at break are key parameters that affect the properties of packaging materials. Through tensile testing, we evaluated the mechanical properties of the biocomposite films, and the results are shown in Fig. 6a. As can be seen from Fig. 6a, the tensile strength (TS) and elongation at break (TB) of the PMG-based biocomposite film are 15.1 MPa and 65.7%, respectively. However, compared with the PMG film, the

addition of commercially available nanocellulose did not significantly increase the stress of the film (17.5 MPa), but the elongation at break reached 89.3%. This is due to the length-diameter ratio and rich hydroxyl group of commercially available nanocellulose, which can form a strong interfacial interaction with the matrix, thereby improving the elongation at break of the membrane.

It can be seen from Fig. 6b that the addition of SR-CNF increases the tensile strength of PNG20 and PNG60 to 24.8 and 26.0 MPa, respectively, while the elongation at break decreases to 80.9% and 83.4%, respectively. These values exceed the tensile strength of St/PVA films prepared using straw-derived cellulose as reported by Sharma et al.[53] and by Ramesh et al.[54] and Arun[55] as reported by mixing nanocellulose extracted from potato peels and coconut shells with PVA (Table S6). In addition, the tensile deformation effect of the film can also be visually visualized from (c) and (d) in Fig. 6.

The preparation of these composite films mainly relies on physical cross-linking, which has relatively low tensile strength and room for improvement compared with chemical cross-linking methods. The tensile strength of thin films is generally determined by the crosslinking density of the network structure, which consists of intermolecular covalent bonds and physical interaction forces, which can be enhanced by the formation of hydrogen bonds between the polyphenolic compounds and the polymer.[56] PNG60 has higher tensile stress due to its more uniform particle size and denser mesh structure. In contrast, the uneven particle size distribution of SR-
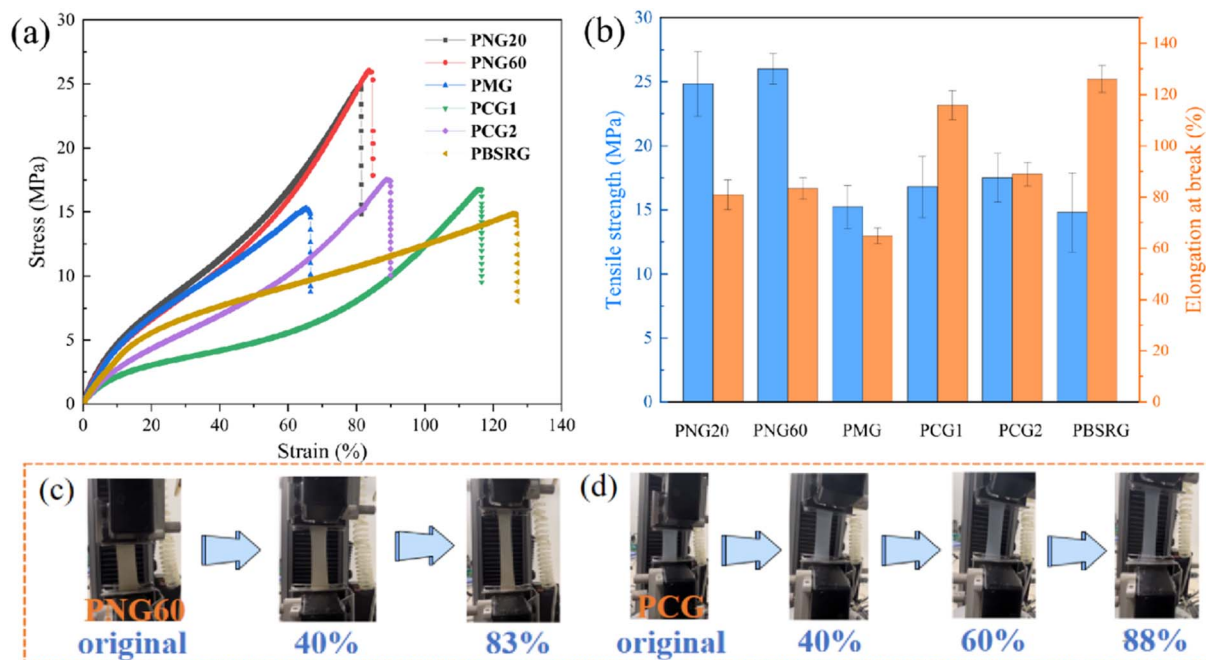
Fig. 6 (a) Stress−strain curves of PNG20, PNG60, PMG, PCG composite films. (b) Tensile strength and elongation at break of composite films. (c) and (d) are the visual tensile deformation effects of PNG60 and PCG films, respectively.

CNFs prepared in PNG20 at low concentrations of OA led to a decrease in mechanical properties,[57] which is consistent with the SEM observations of smaller nanofibers prepared with high concentrations of OA. In addition, the hydrogen bonds formed between the nanocellulose and the PVA contribute to the efficient dispersion of the nanocellulose within the membrane, facilitating the efficient transfer of the load from the matrix to the reinforcement.[58] Nanocellulose acts as an interface connector between the filler and the matrix in the polymer matrix, thereby improving the mechanical properties of the composite film. This improvement in mechanical properties may be due to the molecular interaction between the polymer matrix and the filler.[59] The good dispersion of nanocellulose significantly affects the microstructure and interaction of polymer films, thereby affecting the tensile properties of composite films.[60]

4 Economic cost analysis

In the industrial application of nanocellulose, the cost of raw materials plays a crucial role in achieving large-scale production and sustainable development. SR, a by-product of industrialized and large-scale degumming, offers a stable supply source, abundant yield, and convenient recycling, at a low price of less than \$0.2 per kg^{-1}. In contrast, straw, another type of agricultural waste, has seasonal limitations in yield and is typically only available in large quantities after the annual fall harvest, leading to a collection cost of approximately \$0.4 per kg^{-1}. Wood flour, a waste product from furniture production, can be obtained from large-scale processing plants; however, the lignin contained in it must be removed during the production of nanocellulose, which adds to the economic cost due to the additional solvent required.

Peanut shells, a by-product of cash crop peanuts, can be obtained in large quantities from processing plants but have a higher raw material price of \$2.6 per kg^{-1} compared to bagasse, which is relatively inexpensive at about \$0.6 per kg^{-1}. Despite this, bagasse production is limited by seasonal harvesting, affecting its stability as a feedstock for industrialization. Broadleaf pulp, derived from broadleaf wood, is not seasonally limited in yield and can be produced on a large scale and in batches. Most commercial nanocellulose raw materials are derived from wood pulp, which is rich in cellulose. However, the high cost of raw materials and the economic burden of removing lignin result in a high cost for commercial nanocellulose. It is worth noting that there is no significant difference in the mechanical properties of composite films prepared using SR-CNF compared to commercial nanocellulose. Therefore, SR is an ideal raw material for nanocellulose production due to its environmentally friendly and economical characteristics, stable supply, large quantity, and sustainability.

5 Conclusion

Compared to other nanoscale fibers synthesized using natural raw materials or waste, Nano fibers based on algal residue exhibit significant advantages in terms of yield and cost. Algal residue is an industrial by-product of seaweed gum extraction, which is low in value and inexpensive (<0.2 \$ per kg). This study successfully demonstrated the use of a mild acid pretreatment, assisted by ultrasonic disintegration, to prepare nanofibers with a high yield of 57.3%. The proposed method is both green and energy-efficient, providing a practical way to prepare nanoscale fibers. The study explores the structural, optical, crystalline, and thermal properties of SR-CNF. The concentration of acid is high, which reduces the distribution of ash in the nanofibers,

promotes nanosizing of the fibers, and distributes the average particle size within 200 nm. The average diameter of the prepared SR-CNF was reduced from 957.59 nm to 419.74 nm as the acid concentration increased from 10% to 60%. The SR-CNF exhibited a cellulose I structure, good transparency, thermal stability, and crystallinity, with a crystallinity index of 71.47% and a maximum thermal decomposition temperature of 353.68 °C. Additionally, the SR-CNF demonstrated good optical and thermal stability. The PVA/SR-CNF20/glycerol composite biofilm prepared in this study exhibited good light transmission, a certain level of tensile strength, and an excellent UV shielding effect. It is noteworthy that the UV shielding effect is solely derived from the natural chromophores within the material, without the aid of any external chemical treatment.

With the increase in the concentration of SR-CNF, the tensile strength and energy of the films increased, while the elongation at break decreased. Although the presence of ash content has some impact on the film stress, it does not hinder its potential as a sustainable packaging material. SR-CNF demonstrates the characteristics of an ideal non-renewable filler and renewable green alternative in high-performance applications. The research results indicate that the presence of ash does not affect the performance of SR-CNF, and composite biofilms based on seaweed residue have shown great potential as a new type of polymer film for food packaging.

Author contributions

Shan Jiang conceptualization, methodology, software, formal analysis, writing – original draft. Xincheng Peng: conceptualization, methodology, software, formal analysis, writing – original draft. Yujie Zhang: methodology, software, formal analysis, writing – original draft. Ying Wang: formal analysis, investigation. Hemin Cui: formal analysis, investigation. Ligang Wei: writing – review & editing. Guolin Shao: writing – review & editing, supervision. Na Liu: formal analysis, investigation. Li Wei: formal analysis, investigation.

Conflicts of interest

The authors declare that they have no known competing financial interests or personal relationships that could have appeared to influence the work reported in this paper.

Data availability

The data supporting this article have been included as part of the SI. Supplementary information: Macroscopic and microscopic states and particle size distribution including SR-CNF. See DOI: https://doi.org/10.1039/d5ra03784k.

Acknowledgements

References

1 C. X. Lin, P. Wang, Y. F. Liu, Y. C. Lv, X. X. Ye, M. H. Liu and J. Y. Zhu, *ACS Sustain. Chem. Eng.*, 2023, **11**, 8035–8043.

2 C. Yao, F. Li, T. Chen and Y. Tang, *Ind. Crops Prod.*, 2023, DOI: 10.1016/j.indcrop.2023.117575.

3 J. Fu, Y. Zhou, H. Xie, Q. Duan, Y. Yang, H. Liu and L. Yu, *Int. J. Biol. Macromol.*, 2024, DOI: 10.1016/j.ijbiomac.2024.129837.

4 Y. Yang, L. Zhao, J. Ren and B. He, *Processes*, 2022, DOI: 10.3390/pr10040778.

5 K. V. Neenu, C. D. Midhun Dominic, P. M. S. Begum, J. Parameswaranpillai, B. P. Kanoth, D. A. David, S. M. Sajadi, P. Dhanyasree, T. G. Ajithkumar and M. Badawi, *Int. J. Biol. Macromol.*, 2022, **209**, 1745–1759.

6 S. Jirathampinyo, W. Chumchoochart and J. Tinoi, *Processes*, 2023, DOI: 10.3390/pr11041006.

7 S. Bano and Y. S. Negi, *Carbohydr. Polym.*, 2017, **157**, 1041–1049.

8 J. Wu, X. Du, Z. Yin, S. Xu, S. Xu and Y. Zhang, *Carbohydr. Polym.*, 2019, **211**, 49–56.

9 J. Xu, E. F. Krietemeyer, V. M. Boddu, S. X. Liu and W.-C. Liu, *Carbohydr. Polym.*, 2018, **192**, 202–207.

10 U. P. Agarwal, S. A. Ralph, R. S. Reiner, C. G. Hunt, C. Baez, R. Ibach and K. C. Hirth, *Cellulose*, 2018, **25**, 5791–5805.

11 A. Ait Benhamou, S. Boukind, H. Khalili, A. Moubarik, M. El Achaby, Z. Kassab and H. Sehaqui, *ACS Appl. Polym. Mater.*, 2024, **6**, 2763–2776.

12 S. Prakash, Radha, K. Sharma, S. Dhumal, M. Senapathy, V. P. Deshmukh, S. Kumar, Madhu, T. Anitha, V. Balamurugan, R. Pandiselvam and M. Kumar, *Int. J. Biol. Macromol.*, 2024, **261**, 129456.

13 B. Machado, S. M. Costa, I. Costa, R. Fangueiro and D. P. Ferreira, *Cellulose*, 2024, **31**, 3353–3376.

14 Y. Liu, Y. Chen and H. Qi, *Carbohydr. Polym.*, 2022, DOI: 10.1016/j.carbpol.2022.119729.

15 D. M. S. A. Salem and M. M. Ismail, *Egypt. J. Aquat. Res.*, 2022, **48**, 307–313.

16 Z. Liu, X. Li, W. Xie and H. Deng, *Carbohydr. Polym.*, 2017, **173**, 353–359.

17 M. El Achaby, Z. Kassab, A. Aboulkas, C. Gaillard and A. Barakat, *Int. J. Biol. Macromol.*, 2018, **106**, 681–691.

18 Q. Dai, D. Li, Y. Sun, H. Wang, Y. Lu and D. Yang, *Chemosphere*, 2023, **336**, 139179.

19 B. J. Hardy and A. Sarko, *Polymer*, 1996, **37**, 1833–1839.

20 M. Babicka, M. Wozniak, K. Dwiecki, S. Borysiak and I. Ratajczak, *Molecules*, 2020, DOI: 10.3390/molecules25071544.

21 B. Alonso-Lerma, L. Barandiaran, L. Ugarte, I. Larraza, A. Reifs, R. Olmos-Juste, N. Barruetabena, I. Amenabar, R. Hillenbrand, A. Eceiza and R. Perez-Jimenez, *Commun. Mater.*, 2020, DOI: 10.1038/s43246-020-00055-5.

22 S. Neyertz, A. Pizzi, A. Merlin, B. Maigret, D. Brown and X. Deglise, *J. Appl. Polym. Sci.*, 2000, **78**, 1939–1946.

23 L. F. Zambrano-Mite, Y. Villasana, M. L. Bejarano, C. Luciani, D. Niebieskikwiat, W. Alvarez, D. F. Cueva,

D. Aguilera-Pesantes and L. M. Orejuela-Escobar, *Heliyon*, 2023, DOI: **10.1016/j.heliyon.2023.e17258**.

24 T. Yi, H. Zhao, Q. Mo, D. Pan, Y. Liu, L. Huang, H. Xu, B. Hu and H. Song, *Materials*, 2020, DOI: **10.3390/ma13225062**.

25 R. S. Baghel, C. R. K. Reddy and R. P. Singh, *Carbohydr. Polym.*, 2021, DOI: **10.1016/j.carbpol.2021.118241**.

26 J. Jiang, Y. Zhu, S. Zargar, J. Wu, H. Oguzlu, A. Baldelli, Z. Yu, J. Saddler, R. Sun, Q. Tu and F. Jiang, *Ind. Crops Prod.*, 2021, DOI: **10.1016/j.indcrop.2021.114148**.

27 G. Adriana Bastida, C. Natali Schnell, P. Mocchiutti, Y. Nahun Solier, M. Cristina Inalbon, M. Angel Zanuttini and M. Veronica Galvan, *Nanomaterials*, 2022, DOI: **10.3390/nano12172908**.

28 B. Rietzler and M. Ek, *ACS Sustain. Chem. Eng.*, 2021, **9**, 1398–1405.

29 Y. Zhou, Z. Zhan, H. Liu, H. Xie, J. Fu, L. Chen and L. Yu, *Ind. Crops Prod.*, 2023, DOI: **10.1016/j.indcrop.2023.117095**.

30 Y. Zhao, S. Zhou, X. Xia, M. Tan, Y. Lv, Y. Cheng, Y. Tao, J. Lu, J. Du and H. Wang, *Int. J. Biol. Macromol.*, 2022, **223**, 1126–1137.

31 J. S. Han, S. Y. Kim and Y. B. Seo, *Int. J. Biol. Macromol.*, 2022, **210**, 752–758.

32 B. Basumatary and C. L. Mahanta, *Biomass Convers. Biorefin.*, 2024, **14**, 22297–22314.

33 H. Bian, Y. Yang, P. Tu and J. Y. Chen, *Membranes*, 2022, DOI: **10.3390/membranes12050475**.

34 L. Liu, B. Liu, X. Li, Z. Wang, L. Mu, C. Qin, C. Liang, C. Huang and S. Yao, *Ind. Crops Prod.*, 2023, DOI: **10.1016/j.indcrop.2023.116811**.

35 Q. Chen, G. Ke, Y. Hu, P. Fei and J. Wu, *Cellulose*, 2023, **30**, 1437–1448.

36 M. C. Dias, U. L. Zidanes, C. C. Nemer Martins, A. L. Matos de Oliveira, R. A. Pereira Damasio, J. V. de Resende, E. V. de Barros Vilas Boas, M. N. Belgacem, G. H. Denzin Tonoli and S. R. Ferreira, *Int. J. Biol. Macromol.*, 2022, **213**, 780–790.

37 Z. Chen, Y. Hu, G. Shi, H. Zhuo, M. A. Ali, E. Jamroz, H. Zhang, L. Zhong and X. Peng, *Adv. Funct. Mater.*, 2023, DOI: **10.1002/adfm.202214245**.

38 Z. Wei, D. Wang, Y. Chen, D. Yu, Q. Ding, R. Li and C. Wu, *Cellulose*, 2022, **29**, 3675–3687.

39 K. S. Guiao, C. Tzoganakis and T. H. Mekonnen, *Carbohydr. Polym.*, 2022, DOI: **10.1016/j.carbpol.2022.119543**.

40 V. Balachandrakurup and J. Gopalakrishnan, *Ind. Crops Prod.*, 2022, DOI: **10.1016/j.indcrop.2022.114935**.

41 H. Holilah, H. Bahruji, R. Ediati, A. Asranudin, A. A. Jalil, B. Piluharto, R. E. Nugraha and D. Prasetyoko, *Int. J. Biol. Macromol.*, 2022, **204**, 593–605.

42 K. V. Neenu, C. D. M. Dominic, P. M. S. Begum, J. Parameswaranpillai, B. P. Kanoth, D. A. David, S. M. Sajadi, P. Dhanyasree, T. G. Ajithkumar and M. Badawi, *Int. J. Biol. Macromol.*, 2022, **209**, 1745–1759.

43 S. Zhu, H. Sun, T. Mu, Q. Li and A. Richel, *Food Chem.*, 2023, DOI: **10.1016/j.foodchem.2022.134496**.

44 P. Li, Y. Wang, Q. Hou, H. Liu, H. Lei, B. Jian and X. Li, *Cellulose*, 2020, **27**, 2511–2520.

45 L. Couret, M. Irle, C. Belloncle and B. Cathala, *Cellulose*, 2017, **24**, 2125–2137.

46 R. Khiari, F. Rol, M.-C. B. Salon, J. Bras and M. N. Belgacem, *ACS Sustain. Chem. Eng.*, 2019, **7**, 8155–8167.

47 I. Kouadri and H. Satha, *Ind. Crops Prod.*, 2018, **124**, 787–796.

48 J. Henschen, D. Li and M. Ek, *Carbohydr. Polym.*, 2019, **213**, 208–216.

49 A. J. Onyianta, D. O'Rourke, D. Sun, C.-M. Popescu and M. Dorris, *Cellulose*, 2020, **27**, 7997–8010.

50 Z. Kassab, E. Syafri, Y. Tamraoui, H. Hannache, A. E. K. Qaiss and M. El Achaby, *Int. J. Biol. Macromol.*, 2020, **154**, 1419–1425.

51 N. Blanco-Pascual, M. P. Montero and M. C. Gomez-Guillen, *Food Hydrocolloids*, 2014, **37**, 100–110.

52 M. Safar Razavi Zade, M. H. Aghkhani, M. H. Abbaspour-Fard, F. Hosseini and Z. Qazanfarzadeh, *J. Food Process. Preserv.*, 2021, DOI: **10.1111/jfpp.15926**.

53 M. Sharma, P. Beniwal and A. P. Toor, *Mater. Chem. Phys.*, 2022, DOI: **10.1016/j.matchemphys.2022.126652**.

54 S. Ramesh and P. Radhakrishnan, *Appl. Surf. Sci.*, 2019, **484**, 1274–1281.

55 R. Arun, R. Shruthy, R. Preetha and V. Sreejit, *Chemosphere*, 2022, DOI: **10.1016/j.chemosphere.2021.132786**.

56 Y. Liu, Y. Zhang, M. Zhen, Y. Wu, M. Ma, Y. Cheng and Y. Jin, *Food Hydrocolloids*, 2023, DOI: **10.1016/j.foodhyd.2022.108141**.

57 T. Zhao, M. Tan, Y. Cui, C. Deng, H. Huang and M. Guo, *Polym. Chem.*, 2014, **5**, 4965–4973.

58 W. Jia and Y. Liu, *Cellulose*, 2019, **26**, 8351–8365.

59 U. Montoya, R. Zuluaga, C. Castro, S. Goyanes and P. Ganan, *J. Thermoplast. Compos. Mater.*, 2014, **27**, 413–426.

60 M. Yang, X. Zhang, S. Guan, Y. Dou and X. Gao, *Int. J. Biol. Macromol.*, 2020, **158**, 1259–1267.